# High-energy Neutrino Emission from Espresso-reaccelerated Ions in Jets of Active Galactic Nuclei

Rostom Mbarek[1,2,3] , Damiano Caprioli[1,3] , and Kohta Murase[4,5,6,7]

[1] Department of Astronomy & Astrophysics, University of Chicago, 5640 S Ellis Ave., Chicago, IL 60637, USA; rmbarek@uchicago.edu
[2] Kavli Institute for Cosmological Physics, University of Chicago, Chicago, IL 60637, USA
[3] Enrico Fermi Institute, University of Chicago, Chicago, IL 60637, USA
[4] Department of Physics, The Pennsylvania State University, University Park, Pennsylvania 16802, USA
[5] Department of Astronomy & Astrophysics, The Pennsylvania State University, University Park, Pennsylvania 16802, USA
[6] Center for Multimessenger Astrophysics, Institute for Gravitation and the Cosmos, The Pennsylvania State University, University Park, Pennsylvania 16802, USA
[7] Center for Gravitational Physics, Yukawa Institute for Theoretical Physics, Kyoto 606-8502 Japan

## Abstract

We present a bottom-up calculation of the flux of ultrahigh-energy cosmic rays (UHECRs) and high-energy neutrinos produced by powerful jets of active galactic nuclei (AGNs). By propagating test particles in 3D relativistic magnetohydrodynamic jet simulations, including a Monte Carlo treatment of sub-grid pitch-angle scattering and attenuation losses due to realistic photon fields, we study the spectrum and composition of the accelerated UHECRs and estimate the amount of neutrinos produced in such sources. We find that UHECRs may not be significantly affected by photodisintegration in AGN jets where the *espresso* mechanism efficiently accelerates particles, consistent with Auger's results that favor a heavy composition at the highest energies. Moreover, we present estimates and *upper bounds* for the flux of high-energy neutrinos expected from AGN jets. In particular, we find that (i) source neutrinos may account for a sizable fraction, or even dominate, the expected flux of cosmogenic neutrinos; (ii) neutrinos from the $\beta$-decay of secondary neutrons produced in nucleus photodisintegration end up in the teraelectronvolt to petaelectronvolt band observed by IceCube, but can hardly account for the observed flux; (iii) UHECRs accelerated via the *espresso* mechanism lead to nearly isotropic neutrino emission, which suggests that nearby radio galaxies may be more promising as potential sources. We discuss our results in light of multimessenger astronomy and current/future neutrino experiments.

*Unified Astronomy Thesaurus concepts:* Relativistic jets (1390); Radio jets (1347); Particle astrophysics (96); Ultra-high-energy cosmic radiation (1733); Neutrino astronomy (1100); Cosmological neutrinos (338)

## 1. Introduction

A comprehensive theory that accounts for particle injection, particle acceleration, and spectra of ultrahigh-energy cosmic rays (UHECRs) with energies above $10^{18}$ eV is still lacking. The origin of these particles, however, has been the subject of many theoretical studies that rely mostly on estimates of the maximum energy that particles can achieve in specific environments (Cavallo 1978; Hillas 1984; Alves Batista et al. 2019). In that regard, one of the most promising astrophysical sources of UHECRs are active galactic nucleus (AGN) jets, which satisfy the Hillas criterion up to $10^{20}$ eV, especially if the highest-energy CRs are heavy ions. Additionally, their luminosities can explain the energy injection rate necessary to sustain the UHECR flux (e.g., Katz et al. 2009; Murase & Fukugita 2019; Jiang et al. 2021). Other sources have also been suggested such as newly born millisecond pulsars (e.g., Fang et al. 2012, 2014), $\gamma$-ray bursts (e.g., Vietri 1995; Waxman 1995), engine-driven transrelativistic supernovae including low-luminosity $\gamma$-ray bursts and hypernovae (e.g., Murase et al. 2006; Wang et al. 2008; Zhang & Murase 2019), and tidal disruption events (e.g., Farrar & Piran 2014; Zhang et al. 2017). However, the exact acceleration mechanism boosting UHECRs to their energies in these environments has not been pinned down.

This paper is the third in a series of projects aimed to analyze the promising *espresso* model (Caprioli 2015), checking if it may satisfy all the requirements of a particle acceleration theory and outlining its observational predictions. In essence, the *espresso* framework suggests that UHECRs can be produced in relativistic AGN jets via the reacceleration of galactic cosmic ray (CR) seeds. Such seeds, accelerated in supernova remnants up to a few petaelectronvolts in rigidity, penetrate the highly relativistic regions of the jets and tap into their radial electric field to receive one, or even multiple, $\sim\Gamma^2$ boosts in energy. If the jet is sufficiently powerful with $\Gamma \sim 20-30$, a single shot would allow them to reach UHECR energies. In Mbarek & Caprioli (2019, 2021), the *espresso* mechanism has been tested by propagating particles in high-resolution magnetohydrodynamical (MHD) simulations of AGN jets (Mignone et al. 2007; Rossi et al. 2008). The reacceleration of galactic CR seeds is also promising even for subrelativistic AGN jets that are seen at kpc scales, and the model can fit the Auger spectrum and composition data simultaneously (Kimura et al. 2018).

In Mbarek & Caprioli (2019), hereafter MC19, we found that the spectra, chemical composition, and anisotropy of the reaccelerated particles are qualitatively consistent with UHECR phenomenology. Then, in Mbarek & Caprioli (2021), hereafter MC21, we included sub-grid scattering (SGS) to model small-scale magnetic turbulence that cannot be resolved

by MHD simulations, constraining for the first time one potentially crucial but hard-to-model ingredient. We established the relative importance of *espresso* and stochastic shear acceleration in relativistic jets, finding that strong SGS, on one hand, can promote the injection and acceleration of lower-energy UHECRs, but on the other hand, is irrelevant for the acceleration of the highest-energy CRs, which are invariably *espresso* accelerated in the inner regions of relativistic jets. However, we should also keep in mind that shear acceleration may play a more important role in accelerating particles in subrelativistic jets that are usually seen in kiloparsec scales, especially for Fanaroff–Riley (FR) I galaxies. Overall, we expect the neutrino production to be relatively important in the relativistic spine of the jet, in particular powerful jets seen in FR-II galaxies and flat spectrum radio quasars (FSRQs), where particles are promoted to the highest energies.

In this paper, we evaluate the effects of photodisintegration and high-energy neutrino production in AGN jets within our self-consistent particle acceleration framework. In particular, we investigate how the intense radiation fields of the blazar zone, the broad-line region, and the dusty torus may affect the chemical composition of the accelerated particles. Moreover, modeling UHECR attenuation in a realistic jet environment allows us to calculate the spectrum of high-energy neutrinos produced in these sources. Within our bottom-up approach, we aim to address, with as few assumptions as possible, some key open questions such as the following:

1. What are the effects of losses on *espresso*-accelerated particles in sub-kiloparsec-scale AGN jets?
2. What is the expected spectrum of UHE (ultrahigh-energy) neutrinos produced by a typical AGN jet?
3. If UHECRs are accelerated in AGN jets via the *espresso* mechanism, can they be responsible for the observed IceCube flux, too?

This work would be particularly important to unravel questions associated with UHE neutrinos. UHE neutrinos are created through interactions of UHECRs and are pivotal tools to advance our knowledge of extreme astrophysical environments. Many current and proposed experiments, such as the ANITA Balloon-borne Radio Interferometer (Gorham et al. 2018a, 2018b), its successor PUEO (Abarr et al. 2021), the Askaryan Radio Array (ARA; Allison et al. 2012, 2016), ARIANNA (Barwick et al. 2017), the exciting next-generation IceCube detector, IceCube-Gen2 (IceCube-Gen2 Collaboration et al. 2014), GRAND (Álvarez-Muñiz et al. 2020), RNO-G (Aguilar et al. 2021), BEACON (Wissel et al. 2020), and the proposed POEMMA mission (Olinto et al. 2017), all aim to detect exaelectronvolt neutrinos for the first time. There are many studies that focus on *cosmogenic neutrinos*, i.e., the neutrinos created by UHECRs through interactions with the extragalactic photon background during intergalactic propagation (e.g., Beresinsky & Zatsepin 1969; Yoshida & Teshima 1993; Takami et al. 2009; Heinze et al. 2016; Romero-Wolf & Ave 2018; Das et al. 2019; Heinze et al. 2019; Wittkowski & Kampert 2019). However, UHE *source neutrinos*, i.e., neutrinos produced in or around UHECR accelerators, especially in the presence of extreme photon fields, could also be crucial to unraveling the sites of production of the highest-energy particles in the universe (see Batista et al. 2019, and references therein). This study aims to shed more light on these UHE *source neutrinos*.

In this paper, we propagate particles in an MHD simulation of an AGN jet to keep assumptions to a minimum and find that

particles are *espresso* accelerated (MC19, MC21). The neutrino spectrum that ensues is presented in Section 3.

The paper is organized as follows. In Section 2, we describe our particle acceleration framework, detailing the different interaction routes that lead to losses and neutrino production. In Section 3, we investigate the effects of losses on the UHECR chemical composition and put constraints on the expected *upper bounds* of the neutrino spectrum resulting from UHECR interactions. We also discuss the acceleration mechanism responsible for boosting UHECRs that may contribute to the IceCube flux, and finally we present our conclusions in Section 4.

## 2. Propagating Particles in Realistic Jets

### 2.1. MHD Simulation of a Relativistic Jet

To facilitate the comparison with published results, we model the underlying AGN relativistic jet via the same benchmark simulation used in MC19 and MC21; we refer to those papers for all the details and summarize here the essential information. We consider a 3D relativistic MHD simulation of a powerful AGN jet performed with PLUTO (Mignone et al. 2010), which includes adaptive mesh refinement. The jet, with a magnetization radius $R_{\rm jet}$, is initialized with Lorentz factor $\Gamma_0 = 7$ along the $z$-direction in a box that measures $48R_{\rm jet}$ in the $x$- and $y$-directions and $100R_{\rm jet}$ in the $z$-direction in a grid that has $512 \times 512 \times 1024$ cells with four refinement levels. The jet/ambient density contrast is set to $\psi = 10^{-3}$, and the jet sonic and Alfvénic Mach numbers to $M_s = 3$ and $M_A = 1.67$, respectively. Once the jet has developed, the effective Lorentz factor in the jet spine is $\Gamma_{\rm eff} \sim 3.2$; this value is important to establish how many $\Gamma^2$ shots a particle undergoes during acceleration.

### 2.2. Particle propagation

We propagate $\sim 10^5$ test particles in a snapshot of the benchmark jet with a broad range of initial gyroradii $\mathcal{R}$ and positions. We include the effects of unresolved turbulence by setting the SGS mean free path to be as small as the particle's gyroradius (Bohm diffusion) to maximize the number of particles within the jet spine and boost the efficiency of particle acceleration (see MC21 for more details on the effects of SGS). This prescription maximizes the particles' residence time in the jet (and hence the effects of photon fields), but does not affect particle acceleration at the highest energies, which are invariably accelerated via the SGS-independent *espresso* mechanism (see MC21).

In addition to protons, we consider four different seed ion species, labeled se = [He, C/N/O, Mg/Al/Si, Fe] with effective atomic number $Z_{\rm se} = [2, 7, 13, 26]$ and mass $A_{\rm se} = [4, 14, 27, 56]$, respectively. The energy flux of these seed galactic CRs below the knee is parameterized as follows:

$$\phi_{\rm se}(E) \;=\; K_{\rm se}\!\left(\frac{E}{10^{12}\,{\rm eV}}\right)^{-q_{\rm se}}. \qquad (1)$$

We set the normalizations according to the abundance ratios at $10^{12}$ eV observed in Galactic CRs, such that $K_{\rm se}/K_H \sim [0.46, 0.30, 0.07, 0.14]$. The motivation for using Galactic CR fluxes as fiducial cases hinges on the fact that the knee feature (the maximum seed energy) should be quite independent of the galaxy mass (Caprioli 2015). We acknowledge that the actual
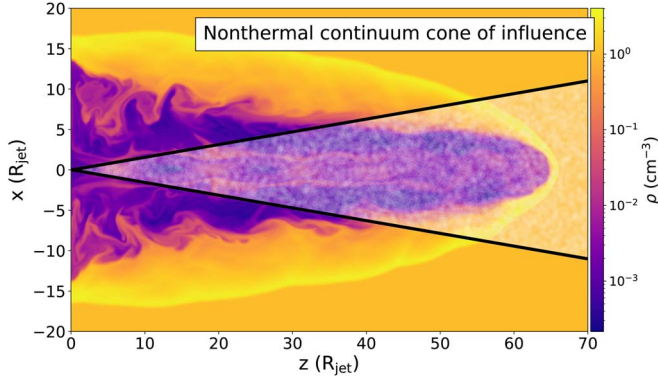
**Figure 1.** Nonthermal continuum cone of influence overlaid on a 2D slice of the density component of the MHD jet. The cone is relativistically beamed at an angle $1/\Gamma_{\rm eff}$, Where $\Gamma_{\rm eff} \sim 3.2$ is the effective Lorentz factor of the jet (See Figure 6 in MC19 for more details). The density is normalized based on the assumptions discussed in Section 2.4.1 to maximize $pp$ interactions.

seed fluxes in AGN hosts may be different due to the different injection and confinement properties of other galaxies but since the chemical enrichment provided by diffusive shock acceleration of seeds in supernova remnants (Caprioli et al. 2010, 2017) is rather universal and since the final UHECR fluxes that we consider are normalized to the observed one, the assumptions above are quite generic. The spectra of different species are calculated as outlined in Appendix A.

Particles are propagated in the MHD simulation even if their gyroradii are smaller than the grid size, which is reasonable as long as a sufficiently small rigidity-dependent time step is used to resolve their gyration; every particle's gyroradius is resolved with *at least* 10 time steps.

### 2.3. Photon Field Prescriptions

On top of the jet structure provided by the MHD simulation, we prescribe external photon fields based on the methods presented in Murase et al. (2014), hereafter MID14. There is ostensible uncertainty in modeling these external components due to the vast AGN diversity, but the systematic approach of MID14 allows us to assess the individual effect of such fields based on the apparent bolometric luminosity of the jet.

We consider five different photon backgrounds of different origin:

(i) Nonthermal emission: This originates from synchrotron and inverse-Compton radiation of relativistic leptons and/or hadronic emission, emerging from the blazar zone, a sub-parsec region close to the base of the jet (see MID14 for more details), where the emission is dominated by X/$\gamma$-rays and is relativistically beamed with an angle $\sim 1/\Gamma$ in the black hole frame. We refer to this broadband emission region as the nonthermal cone of influence (see Figure 1).

(ii) Radiation from the broad-line region (BLR): This is the reprocessed emission from cold gas clumps photoionized by the UV and X-ray produced by the accretion disk. These sub-parsec spherical clumps are located closer to the base of the jet ($<1$ pc away) and have a luminosity $\sim 10\%$ of that of the accretion disk (see MID14).

(iii) IR emission from the dusty torus: This is IR from reprocessed accretion dusty disk radiation with a torus size that can reach $\sim 1$ pc. Following MID14, we model it as a spherical graybody with a temperature of $\sim 500$ K.

(iv) Stellar light: The photons from the host-galaxy stars have been shown to have large energy densities compared to other photon fields at a few hundred parsec, which makes them important targets for accelerated particles in powerful AGN jets. In the remainder of the paper, we will consider the starlight emission profile for Centaurus A as our fiducial case (Tanada et al. 2019).

(v) The cosmic microwave background (CMB) radiation: Besides affecting every particle regardless of its location, accounting for the CMB contribution serves as a benchmark to compare the effects of the prescribed photon fields.

In the remainder of the paper, all photon fields are assumed to be isotropic except for the nonthermal component, which is beamed within a cone of aperture $1/\Gamma_{\rm eff}$, where $\Gamma_{\rm eff}$ is the effective Lorentz factor of the jet. The BLR, IR, and nonthermal contributions have intensities that are inversely proportional to the square of the distance from their emitting regions.

### 2.4. Particle Interactions

When propagating our test particles, at every time step we: (i) calculate the probability of interaction with the thermal plasma (assuming it is electron–proton) and photon fields; (ii) keep track of each particle's atomic mass $A$ and charge $Z$; (iii) monitor secondary particle production including neutrinos and secondary protons. Finally, secondary protons and ions are further propagated until parent and secondary nuclei have traveled a distance of at least 100 $R_{\rm jet}$. Produced neutrinos are assumed to escape without experiencing further interactions; their place of production and escaping direction are recorded, though.

In order to study the effects of UHECR photodisintegration and the resulting neutrino flux, we consider the most relevant attenuation mechanisms, i.e., inelastic proton–proton ($pp$), photomeson production ($p\gamma$), and neutron decay following the photodisintegration of heavy nuclei. More specifically, photomeson production interactions of photons and nucleons also result in the production of pions that subsequently decay to create photons and neutrinos. On the other hand, photodisintegration interactions are nuclear processes that cause the photon-absorbing nucleus to change to another chemical species and release either a proton or a neutron. Table 1 summarizes the interaction routes that lead to neutrinos and the photodisintegration of heavy elements. For simplicity, we ignore the Bethe–Heitler process in this work, which is sufficient for our current purpose. This process can be important for setting the maximum energy only for very powerful blazars (MID14). A more detailed explanation of the interaction probabilities at every time step is included below.

#### 2.4.1. Proton–proton Interactions

Accelerated particles can experience $pp$ scattering to create charged pions and hence $\nu_e$ and $\nu_\mu$ neutrinos. At every time step, depending on the particle's energy $E_p$ and position $x$, there is an interaction probability $P(E_p, x) \sim n(x)\sigma_{pp}(E_p)R_{\rm jet}\Delta t$, where $\sigma_{pp}$ is the $pp$ interaction cross section (Tanabashi et al. 2018), $n$ is the position-dependent density, and $\Delta t$ is the time step. The neutrino spectrum that results from every $pp$ interaction is calculated based on the parameterization by Kelner et al. (2006).
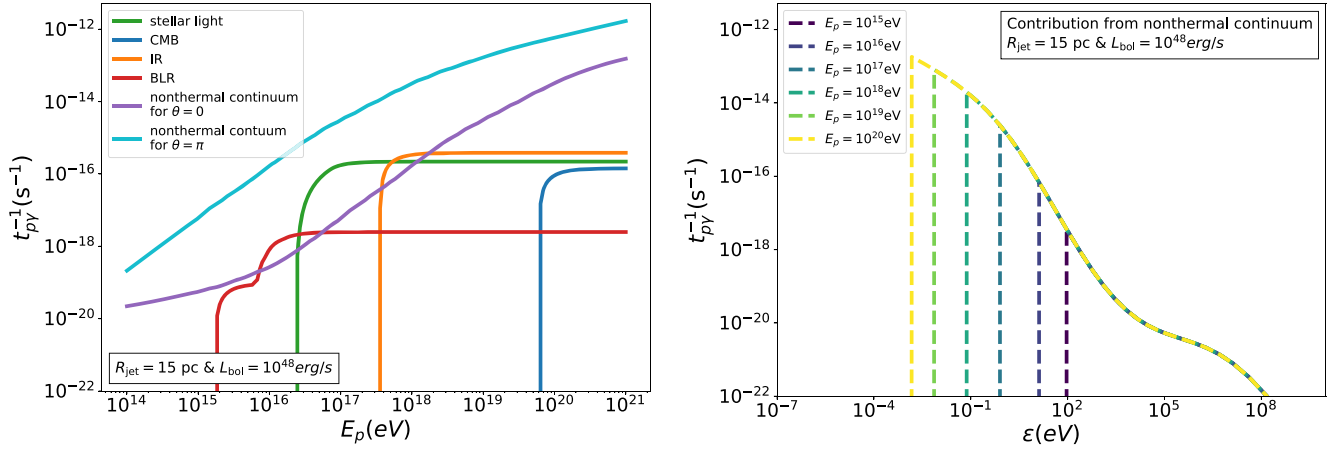
**Figure 2.** Left panel: photomeson cooling time for a proton located at a position (0, 0, 750 pc) for a jet with $R_{jet} = 15$ pc and $L_{bol} = 10^{48}$ erg s$^{-1}$, where $L_{bol}$ is the isotropic-equivalent bolometric luminosity. Contributions from the isotropic photon fields (BLR, IR, stellar light, and CMB) are calculated based on Equation (B3). Contributions from the beamed nonthermal continuum are calculated based on Equation (B5). Here, $\theta$ denotes the angle between the momentum of the proton and the target photon such that $\theta = \pi$ for head-on interactions and $\theta = 0$ for tail-on interactions. Right panel: photomeson cooling time for protons with different energies located at the same position as a function of the photon energy $\epsilon$. This plot only considers head-on interactions ($\theta = \pi$) with the nonthermal continuum as an example.

**Table 1**
Neutrino Production Mechanisms for Protons ($p$) and Nuclei ($N$) of Atomic Mass $A$

| Particle | Process | Reactions | Neutrino Energy fraction |
|---|---|---|---|
| Proton ($p$) | Proton–proton ($pp$) | $p + p \rightarrow p + n + \pi^+ \rightarrow p + n + e^+ + \nu_e + \nu_\mu + \bar{\nu}_\mu$ | $p:\nu \sim 20:1$ |
| | Photomeson ($p\gamma$) | $p + \gamma \rightarrow n + \pi^+ \rightarrow n + e^+ + \nu_e + \nu_\mu + \bar{\nu}_\mu$ | $p:\nu \sim 20:1$ |
| Nucleus ($N$) | Photomeson ($N\gamma$) | $N + \gamma \rightarrow^{A-1} N + n + \pi^+ \rightarrow^{A-1} N + n + e^+ + \nu_e + \nu_\mu + \bar{\nu}_\mu$ | $N:\nu \sim 20$ A:1 |
| | Photodisintegration | $^A N + \gamma \rightarrow^{A-1} N + n \rightarrow^{A-1} N + p + e^- + \bar{\nu}_e$ | $N:\nu \sim 2 \times 10^3$ A:1 |
| | and neutron decay | $^A N + \gamma \rightarrow^{A-1} N + p$ | ... |

**Note.** The last column gives the ratio of the energy of the neutrino with respect to the parent particle (the parameter $\alpha$ is introduced in Appendix D).

Powerful AGN jets are often inside clusters of galaxies (e.g., Begelman et al. 1984; Best et al. 2007; Fang & Murase 2018), so the ambient medium density should reflect that of the intracluster medium, which is of order of $n_{ICM} \sim 10^{-3}$ cm$^{-3}$ (Walg et al. 2013). This reference value is used in Figure 1, which also shows that the jet itself is expected to have an even lower density. Generally, $pp$ interactions inside the AGN jets are not expected to contribute much to the overall neutrino spectrum, although they can be relevant for CRs that have escaped from AGN jets and are confined in clusters (Fang & Murase 2018).

### 2.4.2. Photomeson Production Interactions

At every time step $\Delta t$, a photopion production probability $f_{p\gamma}$ is calculated such that $f_{p\gamma} = t_{p\gamma}^{-1} \Delta t$, where $t_{p\gamma}$ is the photomeson cooling time. A detailed account of $t_{p\gamma}$ calculations for isotropic photon fields and interactions at a known angle for both protons and nuclei with atomic mass $A$ is provided in Appendix B. For $p\gamma$ interactions, we assume a multiplicity of 1 for neutrinos (with energies $E_\nu \sim E_p/20$) produced in one interaction of a relativistic proton, which is valid when the resonance and direct production are relevant. This assumption is valid when target photon spectra are sufficiently soft (Murase et al. 2008).

In general, the cooling time depends on the particle position and on the AGN luminosity; therefore, we cannot use dimensionless quantities but need to introduce physical scales for the magnetic field strength and for the jet size and

luminosity. For instance, the left panel of Figure 2 shows the cooling time for protons of different energies located 750 pc away from the base of the jet along the spine ($z$-direction in Figure 1), for a jet with radius $R_{jet} = 15$ pc and an apparent bolometric luminosity $L_{bol} = 10^{48}$ erg s$^{-1}$. In this characteristic example, we show the contribution from isotropic photon fields (BLR, IR, stellar light, and CMB, as in the legend) and the angle-dependent interactions with the beamed nonthermal continuum (cyan and purple lines). The left panel of Figure 2 shows that the nonthermal contribution provides the shortest photomeson production cooling time (even for tail-on interactions, i.e., $\theta = 0$). These cooling curves depend on the particle position (distance from the base of the jet and position with respect to the nonthermal continuum cone of influence) as will be further discussed below.

The right panel of Figure 2 shows the dependence of the cooling time on the photon energy $\epsilon$ when the proton energy is fixed. Only the nonthermal contribution is shown here for simplicity as it is the dominant photon field in our fiducial cases. We can see that the shortest cooling time—which depends on the proton energy—occurs at the threshold energy $\bar{\epsilon}_{th}$ for photomeson production interactions (see Appendix B for more details). Importantly, the contribution of X/$\gamma$-ray photons with $\epsilon \gtrsim 100$ eV to cooling is only significant for lower-energy protons.

### 2.4.3. Photodisintegration Interactions

On the same photon fields, nuclei with atomic mass $A$ can also undergo photodisintegration with probability $t_{A\gamma}^{-1} \Delta t$ per
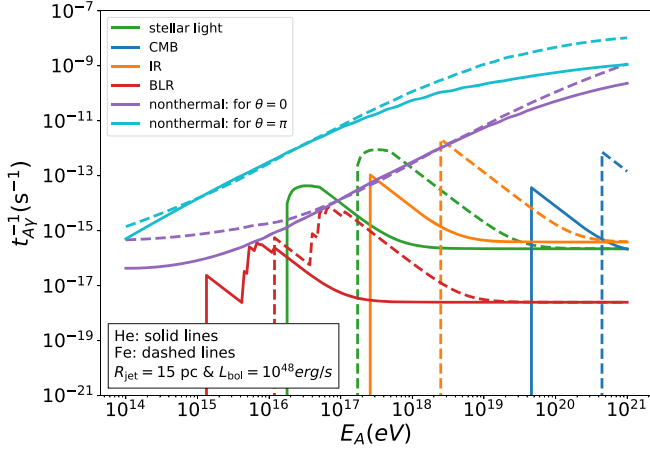
**Figure 3.** Same as the left panel of Figure 2 but for photodisintegration interactions of nuclei with energy $E_A$, including photomeson interactions and interactions based on the GDR photodisintegration total cross section (see Equations (C3) and (C5)). Note that the threshold for He photodisintegration is quite close to that of photomeson production because the plot is a function of $E_A$ and a factor of $A$ must be taken into consideration.

time step. Appendix C details our calculations, in particular, the use of the giant dipole resonance (GDR) cross section (e.g., Murase et al. 2008; Wang et al. 2008) as a fiducial case (see Figure 3). Although this is the simplest application, it is sufficient to demonstrate the effects of photodisintegration in our numerical work. The GDR approximation is valid for soft photon spectra (Murase et al. 2008), and nonthermal photon fields are dominant in our examples. More detailed studies including quasi-deutron emission and fragmentation are left for future work. We also account for photomeson production interactions of heavy nuclei (as described in Equation (B4)), and find that their cooling time is comparable to that of protons. Also for nuclei, the most important photon background is typically the nonthermal component, as shown by a comparison of Figure 3 with Figure 2 and Equation (B4). Higher-energy nuclei are more likely to be photodisintegrated, as expected. Note that the thresholds for photodisintegration interactions for He look quite close to those of photomeson interactions because they are plotted as a function of $E_A$; hence, scaling by the atomic mass A is necessary.

While propagating particles, we keep track of the atomic mass and charge of nuclei, considering that after a photo-disintegration event, the nucleus loses either one neutron or one proton. A neutron produced as a result of photodisintegration decays within a distance $9.15 \, (E_n/10^9 \, \text{GeV})$ kpc (Anchordoqui et al. 2007) to produce one neutrino with energy 0.48 MeV in the neutron rest frame (Murase & Beacom 2010) such that $E_n/E_\nu \approx 2 \times 10^3$ in the lab frame. Since secondary particles cannot achieve energies beyond $\sim 10^{10}$ GeV, we assume that all the secondary neutrons $\beta$-decay and produce neutrinos.

### 2.4.4. Dependence on the Distance from the Central Black Hole

Since different photon backgrounds have different spatial extents, the cooling time for both photodisintegration and $p\gamma$ interactions depend on the magnitude of the distance from the base of the jet, $D$, such that close to the base of the jet $t^{-1} \propto D^{-2}$ where photon fields other than the CMB are most relevant. For a jet with isotropic-equivalent bolometric luminosity $L_{bol} = 10^{45}$ erg s$^{-1}$, nonthermal emission is dominant until $D \sim 3$ kpc, beyond which the CMB becomes

important. Considering that the photon fields we assume are generated close to the base of the jet, CR interactions beyond a few kiloparsec would not increase with large jet extents, usually associated with the more luminous FR-II jets.

### 2.5. From Scale-free MHD Simulations to Realistic Environments

In our simulations, CR gyroradii are normalized to the jet radius $R_{jet}$ and magnetic field $B_0$; therefore, setting a physical value to $R_{jet}$ and $B_0$ is equivalent to associating physical energies to the seed particles of charge $Ze$. In order to calculate the actual neutrino fluxes from realistic AGNs, we need to fix a reference magnetic field and two physical quantities of the jet: its bolometric luminosity, which controls the photon fields, and its radius.

Our simulations have extensively shown that particles are routinely *espresso*-accelerated up to the jet Hillas limit (MC19, MC21). In our 3D relativistic MHD simulations, we launch the jet with $\Gamma = 7$; yet, the effective Lorentz factor of evolved jets turns out to be $\Gamma_{eff}$ approximately a few, too small to promote CR seeds with rigidities of a few petaelectronvolts to actual UHECRs with a single $\Gamma_{eff}^2$ boost. Therefore, in order to achieve realistic UHECR energies, we fix the normalization of our jet radius and magnetization such that CR seeds have rigidities as large as $3 \times 10^{17}$ V, two orders of magnitude above the CR knee. This choice allows us to include the attenuation losses discussed for realistic photon fields and to calculate the fluxes of UHECRs and high-energy neutrinos expected from different types of AGNs.

When contemplating assigning magnetic field, radius, and $L_{bol}$ prescriptions to our jet, one needs to consider different types of radio-loud AGNs, which at minimum can be split into FR-I and FR-II sources. FR-I jets are typically decelerated to nonrelativistic bulk flows within 1 kpc (e.g., Wardle & Aaron 1997; Arshakian & Longair 2004; Mullin & Hardcastle 2009), while FR-II jets, show $\Gamma \gtrsim 10$ at scales of tens of kpc and beyond (e.g., Sambruna et al. 2002; Siemiginowska et al. 2002; Tavecchio et al. 2004; Harris & Krawczynski 2006). The FR dichotomy likely reflects a combination of jet power and ambient density (Bromberg & Tchekhovskoy 2016), and our fiducial jet propagating in a homogeneous density profile may resemble an FR-I jet more than an FR-II one, with a small $R_{jet}/H_{jet}$ ratio, where $H_{jet}$ is the extent of the jet. Yet, in this work we consider a broad range of luminosities that should span the higher-luminosity parameter space. More precisely, we consider the two following cases.

*Case I: FSRQ-like Powerful Jetted AGNs*

As a benchmark for a quite powerful jet of limited ($\sim 1$ kpc) extent, we consider isotropic-equivalent bolometric luminosity $L_{bol} = 10^{48}$ erg s$^{-1}$ with an opening angle $\theta_j \sim 18°$,[8] $R_{jet} = 15$ pc ($H_{jet} \sim 1$ kpc), and $B_0 = 100 \, \mu$G. Such a large magnetic field is routinely inferred in powerful FR-II jets, but should also pertain to the spines of FR-I jets (e.g., Hardcastle et al. 2004; Hawley et al. 2015). This $L_{bol}$ prescription is reminiscent of blazars, including FSRQs and BL Lac objects, that have $L_{bol}$ that go beyond $10^{48}$ erg s$^{-1}$ (e.g., Ghisellini et al. 2010). This should enhance the effects of photodisintegration and the production of neutrinos considering that this $L_{bol}$ is deemed quite large (Ajello et al. 2013; Tadhunter 2016; Blandford et al. 2019; Mingo et al. 2019) and particles propagate closer to the

---

[8] This is important to note considering that the true jet power is $L_{bol}\theta_j^2$.

base of the jet—where most photons are emitted—compared to the expected size of FR-IIs where $H_{jet}$ can reach hundreds of kiloparsec.

*Case II: BL Lac–like Jetted AGNs*

A jet with a more moderate bolometric luminosity $L_{bol} = 10^{45}$ erg s$^{-1}$ with $\theta_j \sim 18°$, $R_{jet} = 1$ pc, and $B_0 = 1.5$ mG is assumed here. Just as in Case I, the strong magnetic field prescription only serves to study the effect of photodisintegration on UHECRs and the production of astrophysical UHE neutrinos. We choose to set the jet radius to 1 pc to further increase the probability of particle interactions as the bulk of the photon field energy is emitted at the base (See Section 2.4.4 for a discussion on the distance dependence), by setting $H_{jet}$ to the smallest FR-I scales (Hawley et al. 2015).

### 2.6. UHECR Injection Spectrum

While the spectrum of UHECRs detected at Earth is measured to be $\propto E^{-2.6}$, the actual spectrum injected by their sources is not well constrained because of the uncertainties in the cosmological distribution of sources and in adiabatic and inelastic losses. While several authors have considered a spectrum of UHECRs injected into intergalactic space, $E^{-q}$, with $q = 2$ (e.g., Waxman 1995; Katz et al. 2009; Aloisio et al. 2011)—which may be valid for protons—more recent Auger data favor harder spectra with $1 \leqslant q \leqslant 1.6$ (e.g., Aloisio et al. 2011; Gaisser et al. 2013; Aloisio et al. 2014; Taylor et al. 2015; Aab et al. 2017a; Jiang et al. 2021) to explain the observed heavy chemical composition.

For steeper proton spectra, the rate of injection of $Q_{UHECR}$ has been calculated to be $EdQ_{UHECR}/dE(q=2) \sim 5 \times 10^{43}$ erg s$^{-1}$ Mpc$^{-3}$ for $E \gtrsim 10^{19}$ eV (e.g., Katz et al. 2009). On the other hand, flatter injection spectra would require a slightly larger rate, such that $EdQ_{UHECR}/dE(q=1) \sim 2 \times 10^{44}$ erg s$^{-1}$ Mpc$^{-3}$ for $E > 10^{16}$ eV (e.g., Aloisio et al. 2014). The energy generation rate density is moderately affected by the composition, and for different compositions from protons to iron nuclei, the differential energy generation rate is $\approx (0.2–2) \times 10^{44}$ erg s$^{-1}$ Mpc$^{-3}$ at $10^{19.5}$ eV (Murase & Fukugita 2019; Jiang et al. 2021).

In this paper, we do not account for propagation effects, and we underline our ignorance of the actual UHECR spectrum by considering injection slopes $1 \leqslant q \leqslant 2$. In the *espresso* framework, the injection spectrum turns out to be flatter than the spectrum of the CR seeds, which should be a power law $\propto E^{-q_{se}}$, with $q_{se} \sim 2 - 2.7$ (Caprioli 2015) because reacceleration tends to push particles close to the jet's Hillas limit (MC19, MC21). It is worth mentioning that $q_{se}$ could approach values of $\sim 2.7$ if we consider relatively short jets like FR-I jets that extend to $\lesssim 10$ kpc, where CRs within the CR halo could be reaccelerated (Kimura et al. 2018). A systematic study of *espresso* acceleration in different kinds of AGN jets is ongoing, but in general, we find that $q - q_{se} \sim 0.5 - 1$, is consistent with the flatter spectra required to explain Auger data (e.g., Aloisio et al. 2014; Taylor et al. 2015). Similar trends are observed in the shear acceleration mechanism, for which it has been shown that Auger data can be quantitatively fitted (Kimura et al. 2018).

In general, the spectrum of secondary particles and UHE neutrinos is a function of $q$; therefore, we show results for different values of $q_{se}$. In the remainder of this paper, we fix the value of the UHECR injection spectrum $q$ such that $1 \leqslant q \leqslant 2$.

## 3. Results

### 3.1. Effects of Energy Losses on UHECR Spectra

Let us start the discussion of our main findings by assessing the role of losses on the spectra of reaccelerated UHECRs. As discussed above, the parameters for Case I are chosen in order to maximize the potential losses for UHECRs: a powerful, yet compact, source would in fact force particles to propagate closer to the AGN and hence be exposed to the bulk of its nonthermal emission (see, e.g., Dermer 2007; Murase et al. 2012). The left panel of Figure 4 shows the average atomic mass and spectrum of UHECRs for Case I, with the contribution of different chemical species and for values $q = 1$, 1.6, and 2. It is worth noting that the UHECR spectrum is not significantly affected by photodisintegration, even with a prescription that may magnify its effects because *espresso* acceleration mainly occurs at scales reaching kiloparsec levels, where the photon density becomes lower than that in the blazar region. Figure 2 indicates that the optical depth at $\sim 10^{20}$ eV is $\sim H_{jet} t_{A\gamma}^{-1}/c \sim 10 < A$, implying that the effective optical depth—taking into account the inelasticity (Murase & Beacom 2010)—is not much larger than unity. Hence, a significant fraction of the heavy nuclei survives losses because seed reacceleration occurs throughout the jet extent, and not just in the blazar region. The light component cuts off at a few times $10^{18}$ eV, and the overall spectrum gets heavier with increasing energy, consistent with Auger observations (Aab et al. 2014a, 2017b; Yushkov 2019). The right panel of Figure 4 breaks down the contribution of each chemical species for $q = 2$ (solid lines, color coded) and also shows the total spectrum for $q = 1$ (dotted line).

Unger et al. (2015) suggested that heavy ions may be photodisintegrated if the UHECR confinement time was increased around sources due to the presence of magnetic irregularities. In this picture, the secondary nuclei originating in these regions would account for the light composition observed below $10^{18}$ eV. Here, we observe a similar phenomenology, in the sense that particle scattering in the cocoon produces a light-element bump of reaccelerated secondary protons around $10^{18}$ eV, provided that the seed spectrum is sufficiently flat. This might correspond to the so-called exaelectronvolt component that is often invoked to fit the low-energy section of the UHECR spectra (e.g., Gaisser et al. 2013; Aloisio et al. 2014). Note that the position of this bump does not depend on the assumed SGS, in that it corresponds to the Hillas limit for protons; also, increased scattering does not significantly increase the confinement time of particles because particles are more likely to escape sideways from the jet as SGS increases (see MC21).

### 3.2. Neutrinos from Interactions of UHECRs Inside Their Sources

#### 3.2.1. UHE Neutrino Flux Expected from a Given Jetted AGN

The black and red curves in Figure 5 show the expected UHECR and neutrino spectra for two different AGN jets (Case I and II, left and right panels, respectively) and for $q = 1$, 2 (dashed, solid lines), as examples of spectral slopes. Extrapolations to other $q$'s are straightforward based on the results in Appendix D.

Two main trends arise, as expected: (1) the neutrino flux increases with increasing jet luminosity (compare left and right
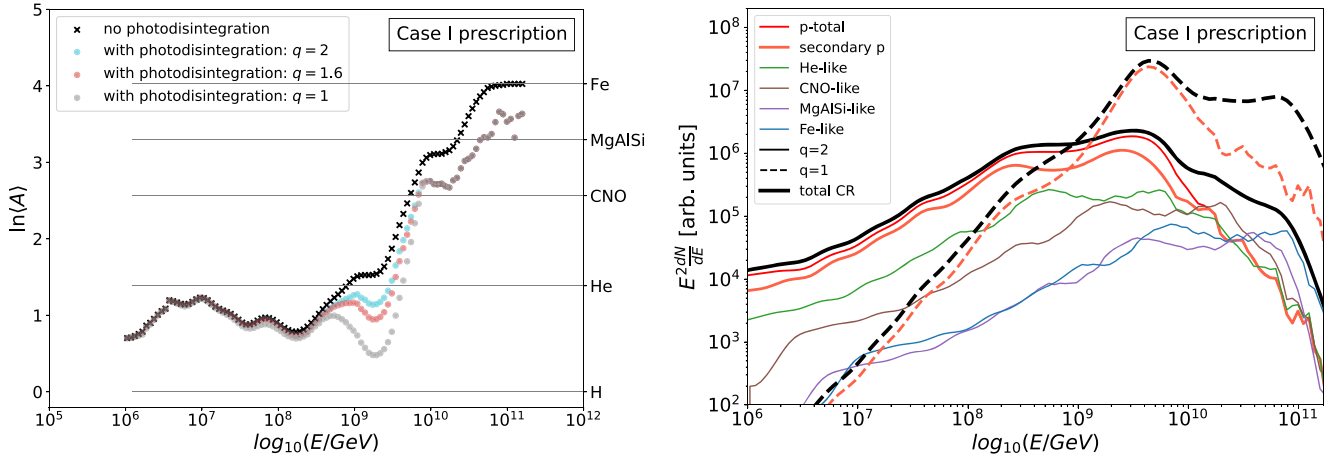
**Figure 4.** Left panel: average atomic mass A as a function of energy for the spectrum from the left panel for Case I prescription. The horizontal solid lines correspond to the atomic masses of the injected chemical species. Right panel: UHECR spectrum including secondary particle spectra. He-like are particles with atomic mass $A \in [3, 8]$; CNO-like with $A \in [9, 18]$; MgAlSi-like with $A \in [19, 35]$; and Fe-like with $A \in [36, 56]$.

panels in Figure 5); (2) the highest-energy neutrinos are produced via photomeson production interactions (thin blue curves), while at lower energies ($\lesssim 10$ PeV), neutrinos from the neutron decay of photodisintegrated UHECRs dominate the flux (thin yellow curves). Finally, we point out that all the neutrinos produced here are from $p\gamma$ interactions; $pp$ collisions are negligible and not visible in the plots. These results do not depend on the level of assumed SGS, since most of the high-energy neutrinos are produced by powerful AGN jets that can be relativistic even at kiloparsec scales, for which CRs are mainly accelerated via the *espresso* mechanism (MC21). We also note that the differences in the total CR spectra between the two panels are quite small for $q = 2$ because the contribution of secondary protons is not as pronounced.

The red lines in Figure 5 are calculated based on the propagation of test particles in our fiducial jet, but it is instructive to also calculate the neutrino spectrum resulting from a much simpler approach that ignores the actual jet structure. Such an analytical *one-zone model* is fully described in Appendix E; in a nutshell, a neutrino flux can be estimated via a rescaling of the UHECR flux based on an effective optical depth $f_{p\gamma}$ for $p\gamma$ interactions, with $f_{p\gamma}$ given by

$$f_{p\gamma}(\gamma) \sim \sigma_{\text{eff}} \, \xi \frac{L_{\epsilon_{\text{typ}}}(\gamma)}{4\pi H_{\text{jet}} c}, \quad (2)$$

where $H_{\text{jet}}$ is the extent of the jet, $\epsilon_{\text{typ}} \approx 0.5 \bar{\epsilon}_{\text{res}}/\gamma$ is the most probable photon energy, $\gamma$ is the particle Lorentz factor, $L_\epsilon$ is the differential luminosity of the jet at $\epsilon$, $\xi$ is the average energy fraction lost to the pion, and $E_\nu = \alpha E$ (see Appendix E and Table 1 for more details). We can then introduce $f_\nu$ (corresponding to the red curves in Figure 5), which can be thought of as an effective optical depth for UHECR interactions. $f_\nu$ globally captures the order of magnitude of the full kinetic approach and can be used to quickly estimate the expected neutrino flux from a given AGN that is active as a UHECR source.

### 3.2.2. Expected Flux of UHE Source Neutrinos

We move now to estimating the overall flux of UHE neutrinos produced by a realistic distribution of the AGN jet luminosity. The energy flux in neutrinos that comes from the convolution over the cosmological distribution of their sources can be expressed as (e.g., Ahlers & Halzen 2014; Murase et al. 2014)

$$E_\nu^2 \Phi_\nu = \frac{c}{4\pi} \int_0^{z_{\text{max}}} \frac{dz}{H(z)} \int d(\ln L) L \frac{d\rho}{dL}(z)$$
$$\times E_\nu^2 \mathcal{J}_\nu[(1 + z)E_\nu, L] \quad (3)$$

where $\rho(z)$ is the number density of sources, $L$ is the AGN jets' luminosity, $H(z) = H_0\sqrt{(1z)^3\Omega_M\Omega_\Lambda}$ is the Hubble parameter, with $\Omega_M \approx 0.3$ and $\Omega_\Lambda \approx 0.7$ for the standard Lambda cold dark matter cosmology, and $H_0 = 70$ km s$^{-1}$ Mpc$^{-1}$ is the Hubble constant. The $E_\nu^2 \mathcal{J}_\nu[(1z)E_\nu, L]$ term is the average neutrino source luminosity.

In this paper, we consider a scenario in which all the UHECRs are produced in environments with intense photon fields, which should get us closer to an upper limit on the possible neutrino flux. Such a flux must be anchored to some expected UHECR luminosity; hence, we scale the $\rho(z)E_\nu^2 \mathcal{J}_\nu$ term with $EdQ_{\text{UHECR}}/dE(E = 10^{19}$ eV$)$ (see Section 2.6), since most CR interactions leading to neutrinos occur at $10^{19}$ eV. See Murase & Beacom (2010) for upper limits on the diffuse neutrino flux from the sources of UHECR heavy nuclei.

Both the photon and the UHECR luminosities for an AGN jet should scale with its bulk power (also see MC19). Ghisellini et al. (2009) found that there may be hints that could relate the jet bulk power to accretion disk luminosity; this study was later complemented by findings from Ghisellini et al. (2014) where it was asserted that there is a clear correlation between the accretion luminosity and $\gamma$-ray jet luminosity. The UHECR injection rate at any redshift can then be written as a function of the local one such that

$$E\frac{dQ_{\text{UHECR}}}{dE}(z, q) = E\frac{dQ_{\text{UHECR}}}{dE}(z = 0, q)\zeta_z(L_{\text{x}}, z), \quad (4)$$

where $\zeta_z$ is a cosmological evolution factor defined in Equation (F1) and $L_{\text{x}}$ the X-ray luminosity of the AGN sources. The prescribed photon fields in our framework are related to $L_{\text{x}}$ such that $L_{\text{bol}}/L_{\text{x}} = 10^{4.21}$ where the constant of proportionality is obtained by modeling the $\gamma$-ray luminosity function through the observed X-ray luminosity (see, e.g., Ueda et al. 2003;
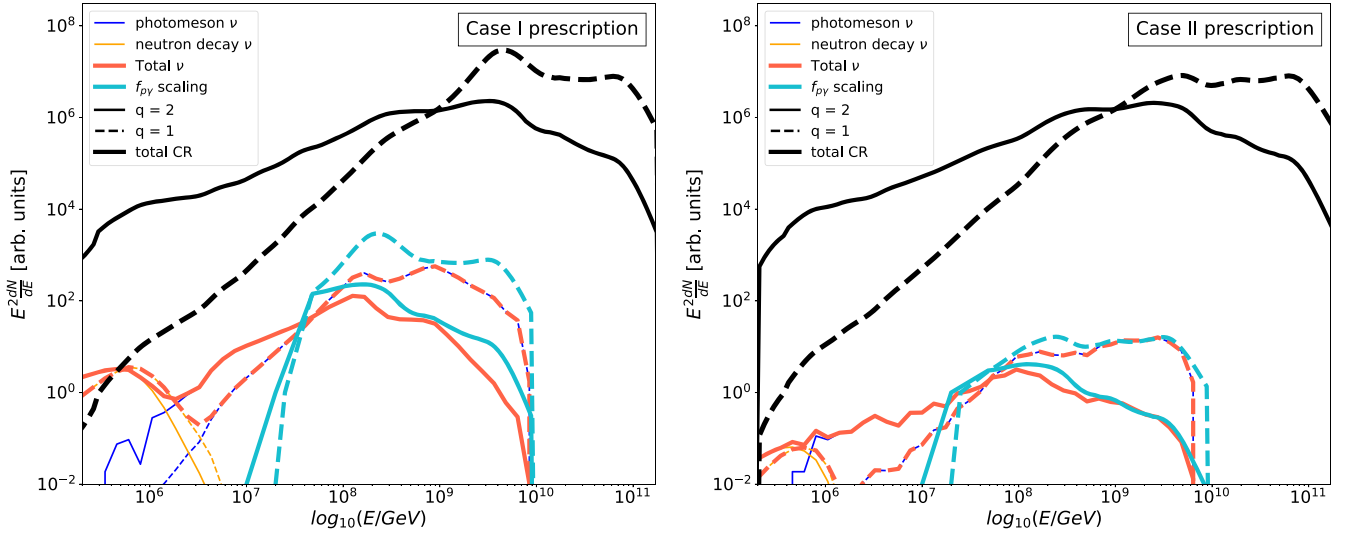
**Figure 5.** Left panel: overall CR spectrum including secondary particles in black for the examples of $q = 1, 2$ assuming the same energy injection rate at $10^{18}$ eV. Note that the CR spectrum is not affected by the bolometric luminosity prescriptions because photodisintegration does not play a major role in this energy range. Blue and orange lines: neutrino spectra that ensued from neutron decay, and $p\gamma$ and $pp$ interactions for different radius and bolometric luminosity prescriptions. The spectra are computed based on the methods presented in Appendices A and D. The teal lines show the expected neutrino based on the $\nu$ scaling from Equation (2). Right panel: same as the left panel but for the Case II prescription.

Inoue & Totani 2009; Harding & Abazajian 2012). This is broadly consistent with the more recent results on the blazar luminosity function (Ajello et al. 2012, 2014).

Assuming that there are different classes of jetted AGNs, we can then rewrite Equation (3) as

$$
\begin{aligned}
E_\nu^2 \Phi_\nu = \frac{c}{4\pi} \int_0^{z_{\max}} \frac{dz}{H(z)} E \frac{dQ_{\mathrm{UHECR}}}{dE}(z = 0, q) \\
\times \sum_i w_i f_\nu(L_i, E, q) \zeta_z(10^{-4.21} L_i, z),
\end{aligned}
\tag{5}
$$

where the weights $w_i$ of the different classes are defined as the relative X-ray injection in cubic megaparsecs of each AGN type:

$$
w_{\log(L_{\mathrm{bol}})} = w(L_{\mathrm{x}}) = \frac{L_{\mathrm{x}} \frac{d\psi}{dL_{\mathrm{x}}}}{\sum_k L_k \frac{d\psi_k}{dL_k}},
\tag{6}
$$

such that $\frac{d\psi}{dL_{\mathrm{x}}}(L_{\mathrm{x}}, z)$ is the $z$-dependent X-ray luminosity function of the AGN sources per luminosity per comoving volume (see MID14 for more details). As discussed in Section 2.6, $EdQ_{\mathrm{UHECR}}/dE$ depends on the injection slope $q$, and in particular, we have that $EdQ_{\mathrm{UHECR}}/dE(z = 0, q = 2) \sim 5 \times 10^{43}$ erg Mpc$^{-3}$ yr$^{-1}$ (Katz et al. 2009) at $\sim 10^{19}$ eV generally assumed for pure proton compositions. For heavier UHECR compositions, a slightly larger injection could be favored such that $EdQ_{\mathrm{UHECR}}/dE(z = 0, \ 0.1 \leqslant q \leqslant 2.7) \sim (0.3 - 2) \times 10^{44}$ erg Mpc$^{-3}$ yr$^{-1}$ at $\sim 10^{19}$ eV (Jiang et al. 2021). Integrated values of the energy generation rate density have also been reported such that $Q_{\mathrm{UHECR}}(z = 0, \ q \leqslant 1.6) \sim 2 \times 10^{44}$ erg Mpc$^{-3}$ yr$^{-1}$ for $E > 10^{16}$ eV $n^{-1}$ (Aloisio et al. 2014) and $Q_{\mathrm{UHECR}}(z = 0, q = 1) \sim 5 \times 10^{44}$ erg Mpc$^{-3}$ yr$^{-1}$ at $\sim 10^{19}$ eV (Aab et al. 2017a). Here, we assume a rate equivalent to $EdQ_{\mathrm{UHECR}}/dE(z = 0, q < 2) = 2 \times 10^{44}$ erg Mpc$^{-3}$ yr$^{-1}$ and $EdQ_{\mathrm{UHECR}}/dE(z = 0, \ q = 2) = 0.5 \times 10^{44}$ erg Mpc$^{-3}$ yr$^{-1}$ at $10^{19}$ eV to maximize UHECR injection.

In this study, we consider contributions from two types of AGN jets with two different isotropic-equivalent bolometric luminosities: (i) FSRQ-like powerful jetted AGNs with $L_{\mathrm{bol}} = L_{48} \sim 10^{48}$ erg s$^{-1}$ (Case I), and (ii) BL Lac–like jetted AGNs with $L_{\mathrm{bol}} = L_{45} \sim 10^{45}$ erg s$^{-1}$ (Case II). We note that the associated $L_{\mathrm{x}} \frac{d\psi}{dL_{\mathrm{x}}} \propto L_{\mathrm{x}}^{-2}$, so the relative contribution of each AGN type in this case is roughly the same, i.e., $w_{45} \sim w_{48}$ and the total energy injected per unit time in UHECRs is comparable in our case (see discussion below). Note that they could, in principle, accelerate particles to different maximum energies (see the discussion in MC21). We finally obtain

$$
\begin{aligned}
E_\nu^2 \phi_\nu \approx \frac{c}{4\pi} \int_0^{z_{\max}} \frac{dz}{H(z)} E \frac{dQ_{\mathrm{UHECR}}}{dE}(q) \\
\times [w_{45} f_\nu(L_{45}, E, q) \zeta_z(10^{-4.21} L_{45}, z) \\
+ w_{48} f_\nu(L_{48}, E, q) \zeta_z(10^{-4.21} L_{48}, z)]
\end{aligned}
\tag{7}
$$

Figure 6 shows the resulting UHE source neutrino fluxes (black lines) based on Equation (7) and expected cosmogenic neutrino fluxes (green and blue lines). The green line shows the expected cosmogenic neutrino flux from radio galaxies assuming an ion composition consistent with ours (taken from Zhang & Murase 2019, where the shear acceleration scenario following Kimura et al. 2018 is considered). The blue bands, on the other hand, show the expected cosmogenic flux for an AGN model that is more proton-rich based on models that fit Auger's spectral features with different confidence levels (Batista et al. 2019). The pink and brown dotted lines show nucleus-survival bounds on the diffuse neutrino flux from sources of UHECR heavy nuclei (Murase & Beacom 2010), which is consistent with the intuition that neutrino production is inefficient in photon-poor environments allowing the survival of nuclei. The yellow data points show the fluxes of the high-energy neutrino events (Kopper 2017). Also shown are the CR data from Auger (Aab et al. 2020), Telescope Array (Jui 2016), and KASCADE-GRANDE (Apel et al. 2013) for reference.

A few points are worth noting.
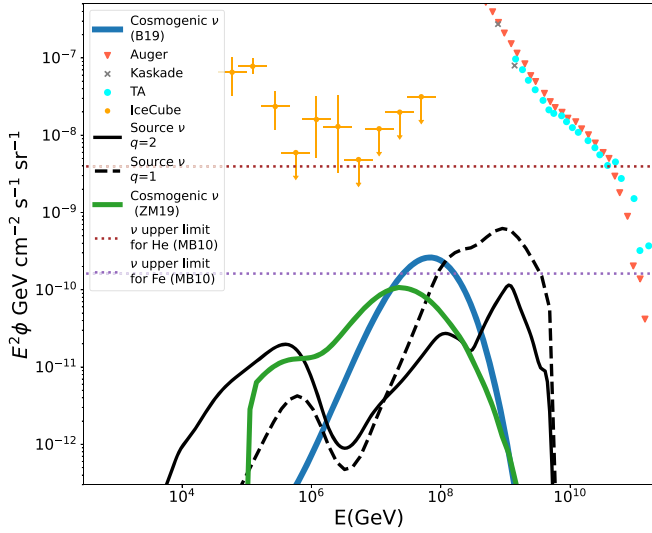
**Figure 6.** Expected upper bounds for the source neutrino flux (black) from UHECR interactions for three different injection slopes $q = 2$ (solid) and $q = 1$ (dashed) including cosmological effects. This flux is compared to the expected cosmogenic neutrino fluxes (green line from Zhang & Murase 2019) for an ion composition similar to ours and a more proton-rich composition (blue bands from Batista et al. 2019) modeled according to an AGN source evolution. The dotted lines show nucleus-survival bounds on the diffuse neutrino flux from sources of UHECR heavy nuclei for helium and iron based on analytical calculations in Murase & Beacom (2010) with $EdQ_{UHECR}/dE(z = 0,$ $q = 2) = 0.6 \times 10^{43}$ erg Mpc$^{-3}$ yr$^{-1}$ and $\xi_z = 7.2$. IceCube neutrino data, along with UHECR data from Auger, KASCADE, and Telescope Array are also included for reference.

1. If injection spectra are sufficiently flat, the flux of source neutrinos may dominate the expected flux of cosmogenic neutrinos (see also Murase et al. 2014; Rodrigues et al. 2021).[9] Even for a moderately flat spectrum of $q = 2$, their relative contribution at $\sim 10^{17}$ eV turns out to be comparable.

2. Given the dependence of the source neutrino flux on $q$ and $\alpha$, neutrinos from the $\beta$ decay of photodisintegration byproducts might become a non-negligible fraction of the flux observed by IceCube below a few petaelectronvolts, although their fluxes are likely to be lower than those from the photomeson production (see also Murase & Beacom 2010).

3. The neutrino fluxes that we obtain for $q = 2$ are lower than the nucleus-survival bounds on the diffuse neutrino flux stemming from UHECRs with $A \geqslant 4$.

### 3.2.3. Upper Limits of the UHE Neutrino Flux in the Reacceleration Scenario

The results shown in Figure 6 should be regarded as close to the *upper limits* of the neutrino flux from AGN jets since we assumed that all UHECRs are produced in jetted AGNs with considerable isotropic-equivalent bolometric luminosities (between $10^{45}$ and $10^{48}$ erg s$^{-1}$).

We remark that:

1. The jet simulations that we consider have a limited extent —consistent with an FR-I jet—with a bolometric luminosity that reaches that of the most powerful blazars.

This further maximizes the effects of the photon fields that are generated close to the base of the jet.
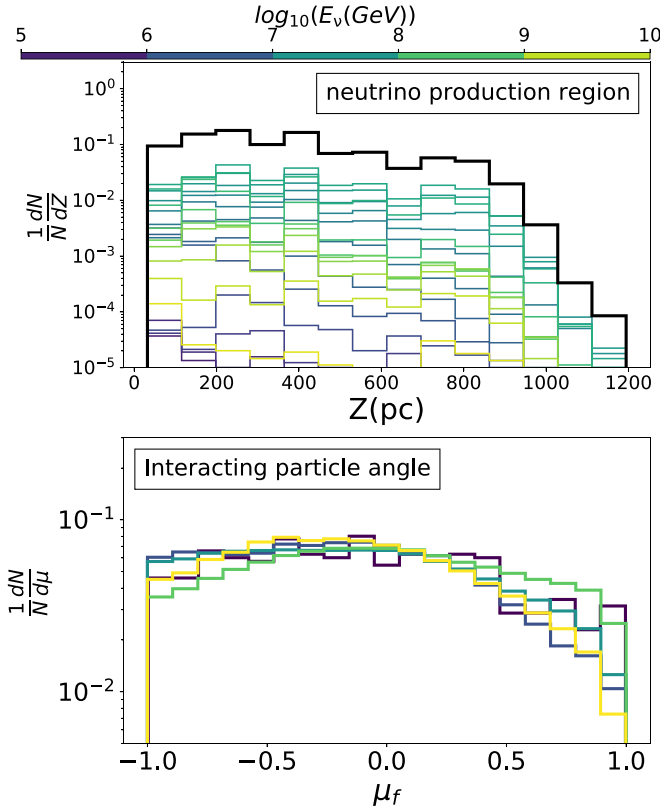
2. Relaxing any of our assumptions would reduce the contribution of the nonthermal photon background to $p\gamma$ collisions; the CMB, BLR, and dusty torus contributions alone would provide a source neutrino flux that would be a few orders of magnitude smaller (see the left panel of Figure 2), subdominant with respect to both the cosmogenic neutrino flux and the astrophysical neutrino flux in the IceCube band.

3. Our results are sensitive to the luminosity function as that directly affects UHECR normalization, the effect of photodisintegration, and the neutrino flux prediction. For example, lower-luminosity AGNs (and/or other classes of sources) may give more contributions to the observed UHECR flux, e.g., via the shear acceleration mechanism because their luminosity density is larger (Ajello et al. 2014). Then the expected neutrino flux would be reduced because the expected neutrino power scales with the bolometric luminosity as shown in Figure 5. Our neutrino flux should still be regarded as an upper limit, since including lower-energy AGNs should not result in a higher neutrino flux.

The results shown in Figure 5 and 6 lead to two very general considerations. On one hand, neutrinos produced by the $\beta$ decay of secondary neutrons should be accounted for when calculating the flux of neutrinos in the petaelectronvolt range. On the other hand, in order to explain the whole IceCube flux with neutrinos from UHECR sources, photodisintegration would need to happen at a much higher rate than what is estimated here, which would be inconsistent with the presence of heavy elements at the highest energies. In other words, the optical depth $f_\nu$ required to produce a sizable source neutrino flux would necessarily lead to the complete photodisintegration of heavy UHECR nuclei; this result is general and independent of the UHECR source or acceleration mechanism. Overall, better UHECR chemical composition measurements and constraints on the UHECR injection slopes may pose more stringent limits on the expected contribution of neutron-decay neutrinos to the observed IceCube flux.

### 3.2.4. Sites of Production and Angular Distribution of Escaping Neutrinos

In our simulations, we keep track of where neutrinos are produced and in which direction they escape. The top panel of Figure 7 shows that a considerable fraction of neutrinos is produced at relatively large distances ($\sim 1$ kpc) away from the base of the jet as a result of two competing effects: on one hand, the photon field intensity declines as $D^{-2}$, and on the other hand, the nonthermal emission cone affects a greater volume as we move away from the base of the jet. We observe similar trends for all of our prescriptions, so we argue that the photodisintegration of heavy UHECR nuclei and neutrino production mainly occur at intermediate distances, not too close to the blazar region but well before the jet's end.

The bottom panel of Figure 7, instead, shows the distribution of the cosines of the final angles of flight of the neutrinos produced through $p\gamma$ interactions and neutron decay for Case I. Neutrinos are released quasi-isotropically, essentially because UHECRs are efficiently isotropized in the cocoon (see also MC19 and MC21).

---

[9] Although beamed neutrino emission is assumed in the previous studies, which is different from our results where the neutrino emission is nearly isotropic (see Section 3.2.4 for more details).

**Figure 7.** Upper panel: final $Z$ position of neutrinos for the Case I prescription to trace the regions where neutrinos are most likely to be produced. Neutrinos are preferentially produced close to the base of a jet within ~800 pc, but a non-negligible fraction of neutrinos is produced at larger distances. Lower panel: distribution of the final angles of escaping neutrinos where $\mu_f$ is the cosine of the angle between the particle momentum and the jet axis. We can see that neutrinos escape the jet *quasi-isotropically*.

This is important for neutrino astronomy because any correlation between neutrino directions of arrival and the AGN population is intrinsically connected to how neutrinos are released from their sources (see also the discussion in Caprioli 2018). If neutrinos are strongly beamed along the jet axis, then they would preferentially be associated with AGN jets that point toward us such as BL Lac objects and FSRQs (i.e., blazars). On the other hand, if the emission were less beamed, we might expect all radio-loud AGNs to contribute to the flux, generally producing a more isotropic signal. Our results suggest that we should receive neutrinos from non-blazar AGNs, too, which makes it harder to assess AGNs as UHE neutrino sources *on a statistical basis*. This prediction is different from the neutrino emission model postulated by Rodrigues et al. (2021). This, however, does not preclude the association of individual events with given sources.

## 4. Conclusions

In this paper, we studied the effects of photodisintegration on UHECRs accelerated in powerful AGN jets and estimate the ensuing flux of high-energy neutrinos. Particles are propagated in a mechanism-agnostic way and we find that UHECRs are generically accelerated via the *espresso* reacceleration of galactic-like CRs (Caprioli 2015)—independently of the jet morphology (MC19) and on the details of particle transport (MC21)—in promising *relativistic* jets, especially for powerful jetted AGN such as FR-II galaxies.

We used a bottom-up approach in which test particles (CR seeds) are propagated in a fiducial 3D MHD simulation of an ultra-relativistic jet, augmented with realistic modeling (á la MID14) of the photon fields responsible for UHECR losses and hence for neutrino production via different channels (see Table 1). We considered different prescriptions for the AGN size and luminosity (Section 2.5) to maximize the interaction rate and, hence, give an optimistic estimate of the expected source neutrino flux, under the additional assumption that powerful jetted AGNs are responsible for the total flux of UHECRs on Earth. We note that relaxing any of these hypotheses would generally lead to a lower neutrino flux.

To summarize, the main findings of this paper are as follows:

1. For typical baryon densities and photon fields, *pp* interactions are negligible with respect to $p\gamma$ collisions; moreover, for powerful jetted AGN the most relevant photon field is provided by the nonthermal jet emission, which dominates over the IR dusty torus emission, the optical stellar light, and even the CMB.

2. UHECRs are not heavily affected by photodisintegration, even in the most luminous AGNs; the spectrum of the highest-energy particles gets heavier with increasing energy, as reported by Auger (Aab et al. 2014b). This situation is different from that in the more compact blazar region (Murase et al. 2012, 2014; Rodrigues et al. 2021).

3. In general, the expected neutrino flux scales with the AGN luminosity and with the slope of the seed and the reaccelerated CR spectra (Figure 5); the rather hard spectra ($q \lesssim 1.5$) required to explain Auger data (see, e.g., Aloisio et al. 2014; Taylor 2014) would maximize the neutrino yield $\geqslant 10^{17}$ eV with respect to softer UHECR spectra.

4. For the most optimistic scenarios (flat UHECR injection spectra), UHE neutrinos produced inside AGN jets may dominate, or at least be comparable to, the expected flux of cosmogenic neutrinos produced during UHECR propagation across the universe (Figure 6).

5. Even if AGNs sustained the totality of the UHECR luminosity of the universe, their steady neutrino emission could not account for the entire IceCube astrophysical neutrino flux (Figure 6). However, a non-negligible fraction of the source neutrinos in the IceCube band may come from the $\beta$-decay of photodisintegration byproducts, rather than from photomeson production.

6. In the reacceleration scenario, neutrinos should be released quasi-isotropically, which strongly suggests that non-blazar jets that correspond to radio galaxies should contribute to the UHE astrophysical neutrino flux. This prediction is different from models of beamed neutrino emission (e.g., Rodrigues et al. 2021).

Note that CR acceleration and neutrino production may occur in different regions. Large-scale jets eventually become subrelativistic, where UHECRs may be accelerated by the stochastic acceleration mechanism (Kimura et al. 2018; Rieger 2019). However, the photon density is so low that neutrino production there was shown to be inefficient (Zhang & Murase 2019). On the other hand, AGNs with large-scale jets are embedded in galaxy groups and clusters, where the CRs escaping from the jets can be confined in the intracluster medium for a cosmological time, in which high-energy neutrinos are produced predominantly via *pp* interactions

(Fang & Murase 2018). We defer to a future study the estimate of the neutrino flux expected from nearby sources, such as M87 and Centaurus A, which may be detectable by current/future experiments even if such moderately powerful AGNs were not contributing substantially to the observed flux of UHECRs.

# Appendix A
## Spectra of Nuclei

We propagate particles of given rigidity $R$, which for different species with different atomic charge $Z$ corresponds to an energy $E = RZ$. The normalizations of the different ion species are chosen according to the abundance ratios at $10^{12}$ eV such that $K = K_{se}/K_H \sim [1, 0.46, 0.30, 0.14]$ for He, CNO, MgAlSi, and Fe respectively. Hence,

$$f(E_i) = K f(ZR), \tag{A1}$$

with $f(R) = f_0 R^{-q}$ where $q$ is the spectral slope. Then,

$$f(E_i) = f_0 K Z^{-q} (E_i)^{-q}, \tag{A2}$$

where $E_i$ is the ion energy and $R$ is the rigidity.

# Appendix B
## Photomeson Production Interactions

We introduce $t_{p\gamma}$ as the cooling time of a proton with energy $E_p$ due to photomeson interactions, i.e.,

$$t_{p\gamma}(E_p) = \frac{E_p}{dE_p/dt} \sim \frac{E_p}{\Delta E_p / \Delta t}. \tag{B1}$$

We follow Stecker (1968) and for an isotropic photon field and obtain

$$t_{p\gamma}^{-1}(\gamma_p) \approx \frac{\xi c}{2\gamma_p^2} \int_{\bar{\epsilon}_{th}/2\gamma_p}^{\infty} d\epsilon \, n_\gamma(\epsilon) \epsilon^{-2} \int_{\bar{\epsilon}_{th}}^{2\gamma_p \epsilon} \epsilon' \sigma(\epsilon') d\epsilon', \tag{B2}$$

where $\epsilon$ is the photon energy in the black hole frame, $\epsilon'$ its energy in the proton frame, $\xi$ is the inelasticity, and $\bar{\epsilon}_{th} \approx 0.15$ GeV is the threshold energy in the proton frame. We integrate over $\epsilon' = \gamma_p \epsilon (1 - \beta \cos \theta)$, where $\theta$ is the angle between the particle momentum vectors in the black hole frame and $\beta \approx 1$. For $0 \leqslant \epsilon' \leqslant 2\gamma_p \epsilon$, we can introduce the effective cross section $\sigma_{eff} = 70\,\mu b$ (Dermer et al. 2014) with $\sigma_{p\gamma}(\bar{\epsilon}) \sim \sigma_{eff} H(\bar{\epsilon} - \bar{\epsilon}_{th})$ and obtain

$$t_{p\gamma}^{-1}(\gamma_p) \sim \sigma_{eff} \xi c \int_{\bar{\epsilon}_{th}/2\gamma_p}^{\infty} d\epsilon \, n_\gamma(\epsilon, d_p) [1 - \frac{\bar{\epsilon}_{th}^2}{4\epsilon^2 \gamma_p^2}], \tag{B3}$$

where $d_p$ expresses the spatial dependence of $n_\gamma$.

When considering interactions between the photons and a nucleus of atomic number $A$ and energy $E_A$, we assume $\sigma_{eff,A} = A\sigma_{eff}$ and $\xi_A = \xi A^{-1}$. Based on Equation (B3), the

cooling time for nuclei $t_{N\gamma}^{-1}$ eventually reads as

$$t_{N\gamma}^{-1}(\gamma_A) \sim \sigma_{eff} \xi c \int_{\bar{\epsilon}_{th}/2\gamma_A}^{\infty} d\epsilon \, n_\gamma(\epsilon, d_p)$$
$$\times \left[ 1 - \frac{\bar{\epsilon}_{th}^2}{4\epsilon^2 \gamma_A^2} \right]; \quad \gamma_A \equiv \frac{E_A}{A m_p c^2}. \tag{B4}$$

Nonthermal emission in jets is typically beamed; hence, the angle $\theta$ between the proton momentum and the target photon is fixed and we can express $t_{p\gamma}^{-1}(\gamma_p)$ for an individual proton interacting with a beamed photon field as

$$t_{p\gamma}^{-1}(\gamma_p) = \xi c (1 - \beta \cos \theta) \int_{\frac{\bar{\epsilon}_{th}}{\gamma_p(1 - \beta \cos \theta)}}^{\infty}$$
$$\times d\epsilon \sigma_{p\gamma}(\epsilon') n_\gamma(\epsilon) = \sigma_{eff} \xi c (1 - \beta \cos \theta)$$
$$\times \int_{\frac{\bar{\epsilon}_t}{\gamma_p(1 - \beta \cos \theta)}}^{\infty} d\epsilon \, n_\gamma(\epsilon) \tag{B5}$$

such that again $\epsilon' = \epsilon \gamma_p (1 - \beta \cos \theta)$.

# Appendix C
## Photodisintegration Interactions Due to the Giant Dipole Resonance

We follow Murase & Beacom (2010) in calculating the photodisintegration interaction time $t_{A\gamma}$ (for an isotropic background), obtaining an expression similar to Equation (B2), with $\gamma$ the ion Lorentz factor

$$t_{A\gamma}^{-1}(\gamma) \approx \frac{c}{2\gamma_A^2} \int_{\bar{\epsilon}_{th}/2\gamma}^{\infty} d\epsilon \, n_\gamma(\epsilon, d_p) \epsilon^{-2} \int_{\bar{\epsilon}_{th}}^{2\gamma\epsilon} \sigma_{A\gamma}(\epsilon') \epsilon' d\epsilon', \tag{C1}$$

where $\sigma_{A\gamma}$ is the GDR photodisintegration total cross section, which reads as (Karakula & Tkaczyk 1993)

$$\sigma_{A\gamma}(\epsilon') = \frac{\sigma_G \epsilon'^2 (\Delta \epsilon'_G)^2}{[\epsilon_G'^2 - \epsilon'^2]^2 \epsilon'^2 (\Delta \epsilon'_G)^2}, \tag{C2}$$

where $\sigma_G = 1.45 \times 10^{-27}\,A$ cm$^2$, $\epsilon'_G = 42.65 A^{-0.21}$ MeV ($0.925\,A^{2.433}$ MeV) for $A > 4$ ($A \leqslant 4$), and $\Delta \epsilon'_G \sim 8$ MeV.

For isotropic photon spectra, we can simplify Equation (C2) by posing $\sigma_{A\gamma} \sim \sigma_G \Delta \epsilon_G' \delta(\epsilon' - \epsilon_G')$. Equation (C1) becomes

$$t_{A\gamma}^{-1}(\gamma) \sim \frac{c\sigma_G}{2\gamma_A^2} \Delta \epsilon'_G \int_{\bar{\epsilon}_{th}/2\gamma}^{\infty} d\epsilon \, n_\gamma(\epsilon, d_p) \epsilon^{-2} \int_{\bar{\epsilon}_{th}}^{2\gamma\epsilon}$$
$$\delta(\epsilon' - \epsilon'_G) \epsilon' d\epsilon' \sim \frac{c\sigma_G}{2\gamma_A^2} \Delta \epsilon'_G \epsilon'_G \theta(\epsilon'_G - \bar{\epsilon}_{th}) \Xi(d_p), \tag{C3}$$

where $\gamma_A = E_A/(m_A c^2)$, with

$$\theta(x) = \begin{cases} 0, & \text{if } x < 0 \\ 1/2, & \text{if } x = 0. \\ 1, & \text{if } x > 0 \end{cases} \tag{C4}$$

We assume that $\epsilon'_G - \bar{\epsilon}_{th} > 0$ where $\bar{\epsilon}_{th}$ is the threshold energy (10 MeV for photodisintegration) and $\epsilon'_G$ is the energy at which the cross section peaks. Also, $\Xi(d_p) = \int_{\bar{\epsilon}_{th}/2\gamma}^{\infty} d\epsilon \, n_\gamma(\epsilon, d_p) \epsilon^{-2} \theta(2\gamma\epsilon - \epsilon'_G)$. For example, if we deal with two prominent BLR emission lines $\epsilon_{HI} = 10.2$ eV and

$\epsilon_{\mathrm{Ly}\alpha} = 40.8$ eV, then

$$\Xi(d_p) = \frac{n_\gamma(\epsilon_{\mathrm{HI}}, d_p)\theta(2\gamma\epsilon_{\mathrm{HI}} - \epsilon'_{\mathrm{G}})}{\epsilon^2_{\mathrm{HI}}} \frac{n_\gamma(\epsilon_{\mathrm{Ly}\alpha}, d_p)\theta(2\gamma\epsilon_{\mathrm{Ly}\alpha} - \epsilon'_{\mathrm{G}})}{\epsilon^2_{\mathrm{Ly}\alpha}}. \tag{C5}$$

For a nucleus interacting with a beamed photon field, the angle $\theta$ between the photon and nucleus momenta is known and we can write $t^{-1}_{A\gamma}(\gamma_p)$ as

$$t^{-1}_{A\gamma}(\gamma_A) = c(1 - \beta\cos\theta)\int^\infty_{\frac{\bar{\epsilon}_{\mathrm{th}}}{\gamma_A(1-\beta\cos\theta)}} d\epsilon\,\sigma_{A\gamma}(\epsilon')n_\gamma(\epsilon), \tag{C6}$$

where $\sigma_{A\gamma}(\epsilon')$ is given by Equation (C2).

## Appendix D
## Spectra of Secondary Nuclei

The spectra of secondary nuclei are intrinsically dependent on the slopes of primary spectra, which in turn depend on the slope of the seed spectrum. Let us consider primary spectra as power laws in energy $f(E) = f_0 E^{-q}$. For the photodisintegration process, under the GDR approximation, the particle number conservation is justified, in which we get

$$f(E)\,dE = f'(E')\,dE', \tag{D1}$$

where $E$ is the energy of the primary nucleus and $E' = \alpha E$ is the energy of the secondary particle. For example, for a secondary nucleus we have $\alpha \approx (A-1)/A$ while $\alpha \approx 1/A$ for a secondary nucleon.

Then $dE' = \alpha\,dE$ and we obtain

$$f'(E') = f(E)\frac{dE}{dE'} = f_0\frac{E^{-q}}{\alpha}, \tag{D2}$$

and therefore,

$$f'(E') = f_0(E')^{-q}\alpha^{q-1} = f_0 E'^{-q}\alpha^{q-1}. \tag{D3}$$

And finally,

$$f_s(E_s)/f(E_s) = f_0 E_s^{-q}\alpha^{q-1}/f(E_s) = \alpha^{q-1}. \tag{D4}$$

where $E_s$ is the energy of the secondary nucleus or nucleon. Eventually, the relative normalization of primary and secondary spectra reads as $f_s(E_s)/f(E_s) = \alpha^{q-1}$.

## Appendix E
## Spectra of Secondary Neutrinos and Scaling

We consider the photomeson optical depth $f_{p\gamma}$—a proxy for the neutrino production efficiency produced through photomeson production interactions—to estimate the expected astrophysical UHE neutrino spectrum based on the average bolometric luminosity and extent of the jet in the black hole frame. Primary spectra are expressed as power laws in energy $f(E) = f_0 E^{-q}$, and as a result, the number of primary particles is not the same as that of secondary particles. Using $f_{p\gamma}$ we write

$$E^2_\nu f_\nu(E_\nu) \approx \frac{3}{8}f_{p\gamma}(E)E^2 f(E), \tag{E1}$$

where $E$ is the energy of the primary particle, $E_\nu = \alpha E$ is the typical energy of the secondary neutrino, and $\alpha$ can be read in the last column of Table 1 for the different processes that yield neutrinos. While computing the expected neutrino flux, we

need to account for a factor of $1/2$ that comes from the charged-to-neutral pion ratio, and another factor of $3/4$ stemming from pion and muon decay. Then we have

$$f_\nu(E')/f(E') \approx \frac{3}{8}f_{p\gamma}(E'/\alpha)\alpha^{q-2}. \tag{E2}$$

Since UHECRs up the jet's Hillas limit are *espresso*-accelerated, we can estimate their propagation time $t_{\mathrm{prop}}$ to be close to ballistic such that $t_{\mathrm{prop}} \sim \frac{H_{\mathrm{jet}}}{c}$. The effective optical depth $f_{p\gamma}$ can then be estimated as

$$f_{p\gamma}(E) \approx \langle t^{-1}_{p\gamma}(E)\rangle t_{\mathrm{prop}} \sim H_{\mathrm{jet}}\langle n_\gamma(E)\rangle\sigma_{\mathrm{eff}}\xi, \tag{E3}$$

where

$$\langle n_\gamma(E)\rangle \sim \frac{\epsilon_{\mathrm{typ}}L_{\epsilon_{\mathrm{typ}}}}{4\pi c}\frac{1}{\epsilon_{\mathrm{typ}}}\frac{1}{H^2_{\mathrm{jet}}}, \tag{E4}$$

where $\epsilon_{\mathrm{typ}}$ is the most likely photon energy, and $\epsilon_{\mathrm{typ}}$ depends on the considered particle energy such that $\epsilon_{\mathrm{typ}} \sim 0.5\bar{\epsilon}_{\mathrm{res}}/\gamma$ where $\bar{\epsilon}_{\mathrm{res}} \sim 0.34$ GeV is the resonance energy and $\gamma = E/m_A c^2$ is the Lorentz factor of a particle with energy $E$. Note that $\langle n_\gamma(E)\rangle$ is energy dependent. For example, $\epsilon L_\epsilon \propto \epsilon^{2-\beta}$ (with $\beta \gtrsim 1$), we have $\langle n_\gamma(E)\rangle \propto E^{\beta-1}$.

Finally, we get an estimate for $E^2_\nu F_{\mathrm{UHE}\nu}(E_\nu)$ such that

$$E^2_\nu F_{\mathrm{UHE}\nu}(E_\nu) \sim \frac{3}{8}\sigma_{\mathrm{eff}}\xi\frac{L_{\epsilon_{\mathrm{typ}}}(E)}{4\pi H_{\mathrm{jet}}c}E^2 F_{\mathrm{UHECR}}(E). \tag{E5}$$

In the example shown in the left panel of Figure 4, $L_{\mathrm{bol}} = 10^{48}$ erg s$^{-1}$, $H_{\mathrm{jet}} \sim 1$ kpc, and $\gamma > 10^7$ so $\epsilon_{\mathrm{m}} \sim 15$ eV in the black hole frame; the values of $\alpha$, $\sigma_{\mathrm{eff}}$, and $\xi$ are discussed in more detail in Appendix B.

## Appendix F
## Cosmological Evolution of AGN

Following Ueda et al. (2003), Inoue & Totani (2009), Harding & Abazajian (2012), and MID14, We set the cosmological evolution factor $\zeta_z(L_{\mathrm{x}}, z)$, where $z$ is the redshift and $L_{\mathrm{x}}$ is the X-ray luminosity of the source

$$\zeta_z(L_{\mathrm{x}}, z) = \begin{cases} (1z)^{4.23} & \text{if } z \leqslant z_l(L_{\mathrm{x}}) \\ [1z_l(L_{\mathrm{x}})]^{4.23}\left[\dfrac{1z}{1z_l(L_{\mathrm{x}})}\right]^{-1.5}, & \text{if } z > z_l(L_{\mathrm{x}}) \end{cases} \tag{F1}$$

with

$$z_l(L_{\mathrm{x}}) = \begin{cases} z_c & \text{if } L_a \leqslant L_{\mathrm{x}} \\ z_c(L_{\mathrm{x}}/L_a)^{0.335} & \text{if } L_a > L_{\mathrm{x}} \end{cases},$$

such that $z_c = 1.9$ and $L_a = 10^{44.6}$ erg s$^{-1}$.

## ORCID iDs

Rostom Mbarek ● https://orcid.org/0000-0001-9475-5292
Damiano Caprioli ● https://orcid.org/0000-0003-0939-8775
Kohta Murase ● https://orcid.org/0000-0002-5358-5642

## References

Aab, A., Abreu, P., Aglietta, M., et al. 2014a, PhRvD, 90, 122006
Aab, A., Abreu, P., Aglietta, M., et al. 2014b, PhRvD, 90, 122005
Aab, A., Abreu, P., Aglietta, M., et al. 2017a, JCAP, 2017, 038

Aab, A., Abreu, P., Aglietta, M., et al. 2017b, Sci, 357, 1266
Aab, A., Abreu, P., Aglietta, M., et al. 2020, PhRv, 125, 121106
Abarr, Q., Allison, P., Ammerman Yebra, J., et al. 2021, JInst, 16, P08035
Aguilar, J. A., Allison, P., Beatty, J. J., et al. 2021, JInst, 16, P03025
Ahlers, M., & Halzen, F. 2014, PhRv, 90, 043005
Ajello, M., Romani, R. W., Gasparrini, D., et al. 2013, ApJ, 780, 73
Ajello, M., Romani, R. W., Gasparrini, D., et al. 2014, ApJ, 780, 73
Ajello, M., Shaw, M. S., Romani, R. W., et al. 2012, ApJ, 751, 108
Allison, P., Auffenberg, J., Bard, R., et al. 2012, APh, 35, 457
Allison, P., Bard, R., Beatty, J. J., et al. 2016, PhRvD, 93, 082003
Aloisio, R., Berezinsky, V., & Blasi, P. 2014, JCAP, 10, 20
Aloisio, R., Berezinsky, V., & Gazizov, A. 2011, APh, 34, 620
Álvarez-Muñiz, J., Alves Batista, R., & Balagopal, V. A 2020, SCPMA, 63, 219501
Alves Batista, R., Biteau, J., Bustamante, M., et al. 2019, FrASS, 6, 23
Anchordoqui, L. A., Beacom, J. F., Goldberg, H., Palomares-Ruiz, S., & Weiler, T. J. 2007, PhRvD, 75, 063001
Apel, W. D., Arteaga-Velazquez, J. C., Bekk, K., et al. 2013, APh, 47, 54
Arshakian, T. G., & Longair, M. S. 2004, MNRAS, 351, 727
Barwick, S. W., Besson, D. Z., Burgman, A., et al. 2017, APh, 90, 50
Batista, R. A., de Almeida, R. M., Lago, B., & Kotera, K. 2019, JCAP, 2019, 002
Begelman, M. C., Blandford, R. D., & Rees, M. J. 1984, RvMP, 56, 255
Beresinsky, V. S., & Zatsepin, G. T. 1969, PhLB, 28, 423
Best, P. N., Von Der Linden, A., Kauffmann, G., Heckman, T. M., & Kaiser, C. R. 2007, MNRAS, 379, 894
Blandford, R., Meier, D., & Readhead, A. 2019, ARA&A, 57, 467
Bromberg, O., & Tchekhovskoy, A. 2016, MNRAS, 456, 1739
Caprioli, D. 2015, ApJL, 811, L38
Caprioli, D. 2018, NPPP, 297–299, 266
Caprioli, D., Amato, E., & Blasi, P. 2010, APh, 33, 160
Caprioli, D., Yi, D. T., & Spitkovsky, A. 2017, PhRvL, 119, 171101
Cavallo, G. 1978, A&A, 65, 415
Das, S., Razzaque, S., & Gupta, N. 2019, PhRvD, 99, 083015
Dermer, C. D. 2007, arXiv:0711.2804
Dermer, C. D., Murase, K., & Inoue, Y. 2014, JHEAp, 29, 3
Fang, K., Kotera, K., Murase, K., & Olinto, A. V. 2014, PhRvD, 90, 103005
Fang, K., Kotera, K., & Olinto, A. V. 2012, ApJ, 750, 118
Fang, K., & Murase, K. 2018, NatPh, 14, 396
Farrar, G. R., & Piran, T. 2014, arXiv:1411.0704
Gaisser, T. K., Stanev, T., & Tilav, S. 2013, FrPhy, 8, 748
Ghisellini, G., Tavecchio, F., Foschini, L., et al. 2010, MNRAS, 402, 497
Ghisellini, G., Tavecchio, F., & Ghirlanda, G. 2009, MNRAS, 399, 2041
Ghisellini, G., Tavecchio, F., Maraschi, L., Celotti, A., & Sbarrato, T. 2014, Natur, 515, 376
Gorham, P. W., Allison, P., Banerjee, O., et al. 2018a, PhRvD, 98, 022001
Gorham, P. W., Rotter, B., Allison, P., et al. 2018b, PhRvL, 121, 161102
Hardcastle, M. J., Harris, D. E., Worrall, D. M., & Birkinshaw, M. 2004, ApJ, 612, 729
Harding, J. P., & Abazajian, K. N. 2012, JCAP, 2012, 026
Harris, D. E., & Krawczynski, H. 2006, ARA&A, 44, 463
Hawley, J. F., Fendt, C., Hardcastle, M., Nokhrina, E., & Tchekhovskoy, A. 2015, SSRv, 191, 441
Heinze, J., Boncioli, D., Bustamante, M., & Winter, W. 2016, ApJ, 825, 122
Heinze, J., Fedynitch, A., Boncioli, D., & Winter, W. 2019, ApJ, 873, 88

Hillas, A. M. 1984, ARA&A, 22, 425
IceCube-Gen2 Collaboration, Aartsen, M. G., et al. 2014, arXiv:1412.5106
Inoue, Y., & Totani, T. 2009, ApJ, 702, 523
Jiang, Y., Zhang, B. T., & Murase, K. 2021, PhRv, 104, 043017
Jui, C. 2016, PoS (ICRC 2015), 236, 035
Karakula, S., & Tkaczyk, W. 1993, APh, 1, 229
Katz, B., Budnik, R., & Waxman, E. 2009, JCAP, 2009, 020
Kelner, S. R., Aharonian, F. A., & Bugayov, V. V. 2006, PhRv, 74, 034018
Kimura, S. S., Murase, K., & Zhang, B. T. 2018, PhRvD, 97, 023026
Kopper, C. & IceCube Collaboration 2017, PoS (ICRC 2017), 301, 981
Mbarek, R., & Caprioli, D. 2019, ApJ, 886, 8
Mbarek, R., & Caprioli, D. 2021, ApJ, 921, 85
Mignone, A., Bodo, G., Massaglia, S., et al. 2007, ApJS, 170, 228
Mignone, A., Rossi, P., Bodo, G., Ferrari, A., & Massaglia, S. 2010, MNRAS, 402, 7
Mingo, B., Croston, J. H., Hardcastle, M. J., et al. 2019, MNRAS, 488, 2701
Mullin, L. M., & Hardcastle, M. J. 2009, MNRAS, 398, 1989
Murase, K., & Beacom, J. F. 2010, PhRv, 81, 123001
Murase, K., Dermer, C. D., Takami, H., & Migliori, G. 2012, ApJ, 749, 63
Murase, K., & Fukugita, M. 2019, PhRvD, 99, 063012
Murase, K., Inoue, Y., & Dermer, C. D. 2014, PhRv, 90, 023007
Murase, K., Ioka, K., Nagataki, S., & Nakamura, T. 2006, ApJL, 651, L5
Murase, K., Ioka, K., Nagataki, S., & Nakamura, T. 2008, PhRv, 78, 023005
Olinto, A. V., Adams, J. H., Aloisio, R., et al. 2017, PoS (ICRC 2017), 301, 542
Rieger, F. 2019, Galax, 7, 78
Rodrigues, X., Heinze, J., Palladino, A., van Vliet, A., & Winter, W. 2021, PhRv, 126, 191101
Romero-Wolf, A., & Ave, M. 2018, JCAP, 2018, 025
Rossi, P., Mignone, A., Bodo, G., Massaglia, S., & Ferrari, A. 2008, A&A, 488, 795
Sambruna, R. M., Maraschi, L., Tavecchio, F., et al. 2002, ApJ, 571, 206
Siemiginowska, A., Bechtold, J., Aldcroft, T. L., et al. 2002, ApJ, 570, 543
Stecker, F. W. 1968, PhRv, 21, 1016
Tadhunter, C. 2016, A&ARv, 24, 10
Takami, H., Murase, K., Nagataki, S., & Sato, K. 2009, APh, 31, 201
Tanabashi, M., Hagiwara, K., Hikasa, K., et al. 2018, PhRvA, 98, 030001
Tanada, K., Kataoka, J., & Inoue, Y. 2019, ApJ, 878, 139
Tavecchio, F., Maraschi, L., Sambruna, R. M., et al. 2004, ApJ, 614, 64
Taylor, A. M. 2014, APh, 54, 48
Taylor, A. M., Ahlers, M., & Hooper, D. 2015, PhRvD, 92, 063011
Ueda, Y., Akiyama, M., Ohta, K., & Miyaji, T. 2003, ApJ, 598, 886
Unger, M., Farrar, G. R., & Anchordoqui, L. A. 2015, arXiv:1505.02153
Vietri, M. 1995, ApJ, 453, 883
Walg, S., Achterberg, A., Markoff, S., Keppens, R., & Meliani, Z. 2013, MNRAS, 433, 1453
Wang, X.-Y., Razzaque, S., & Meszaros, P. 2008, ApJ, 677, 432
Wardle, J. F. C., & Aaron, S. E. 1997, MNRAS, 286, 425
Waxman, E. 1995, PhRvL, 75, 386
Wissel, S., Romero-Wolf, A., Schoorlemmer, H., et al. 2020, JCAP, 2020, 065
Wittkowski, D., & Kampert, K. H. 2019, MNRAS: Lett., 488, L119
Yoshida, S., & Teshima, M. 1993, PThPh, 89, 833
Yushkov, A. 2019, PoS (ICRC2019), 358, 482
Zhang, B. T., & Murase, K. 2019, PhRvD, 100, 103004
Zhang, B. T., Murase, K., Oikonomou, F., & Li, Z. 2017, PhRvD, 96, 063007